Improving the retrieval of offshore-onshore correlation functions with machine learning

Loïc Viens [1] and Tomotaka Iwata[1]

[1]Disaster Prevention Research Institute, Kyoto University

This paper is a non-peer reviewed preprint submitted to EarthArXiv and has been submitted to Journal of Geophysical Research: Solid Earth for peer review.

Key Points:

- Machine learning is used to improve the retrieval of offshore-onshore deconvolution functions (DFs)
- Typhoons and storms play an important role in the retrieval of clear offshore-onshore DFs
- DFs retrieved with our method are used to better simulate the long-period ground motions from subduction earthquakes

Corresponding author: Loïc Viens, `viens.loic.58r@st.kyoto-u.ac.jp`

Abstract

The retrieval of reliable offshore-onshore correlation functions is critical to improve our ability to predict long-period ground motions from megathrust earthquakes. However, localized ambient seismic field sources between offshore and onshore stations can bias correlation functions and generate non-physical arrivals. We present a two-step method based on unsupervised learning to improve the quality of correlation functions calculated with the deconvolution method (e.g., deconvolution functions, DFs). For a DF dataset calculated between two stations over a long time period, we first reduce the dataset dimensions using the Principal Component Analysis and cluster the features of the low-dimensional space with a Gaussian mixture model. We stack the DFs belonging to each cluster together and select the best stacked DF. We apply our technique to DFs calculated every 30 minutes between an offshore station located on top of the Nankai Trough, Japan, and 77 onshore receivers. Our method removes spurious arrivals and improves the signal-to-noise ratio of the DFs. Most 30-min DFs selected by our clustering method are generated during extreme meteorological events, such as typhoons. To demonstrate that the DFs obtained with our method contain reliable phases and amplitudes, we use them to simulate the long-period ground motions from a M_{w} 5.8 earthquake, which occurred near the offshore station. Results show that the earthquake long-period ground motions are accurately simulated. Our method can easily be used as an additional processing step when calculating offshore-onshore DFs, and offers a way to improve the prediction of long-period ground motions from potential megathrust earthquakes.

Plain Language Summary

Seismic waves from subduction earthquakes are generally characterized by a strong and elongated long-period component due to their propagation through complex velocity structures such as accretionary wedges. Seismic interferometry, which consists of cross-correlating continuous ambient seismic field signals at two seismic stations, can be used to retrieve the wave propagation between the two sensor's locations. However, the retrieval of clear wave propagation between offshore and onshore stations is difficult due to the characteristics of the ambient seismic field. We develop a method based on unsupervised learning to improve the quality of correlation functions between offshore and onshore sites. We apply our method to correlation functions calculated between an offshore station on top of the Nankai Trough, Japan, and surrounding onshore stations. The correlation functions retrieved with our method have a higher signal-to-noise ratio and better simulate the ground motions from a M_{w} 5.8 earthquake, which occurred along the Nankai Trough. Improving our ability to retrieve accurate wave propagation between offshore and onshore stations is critical to better predict the long-period ground motion from potential megathrust earthquakes, which are likely to happen in numerous subduction zones worldwide in the near future.

1 Introduction

Seismic interferometry is a well established method used to gain geophysical information about the Earth's subsurface. By cross-correlating ambient seismic field time series recorded by a pair of seismometers, the seismic wave propagation between the two sensor's locations can be retrieved. Theoretical studies demonstrated that for homogeneously distributed ambient seismic field sources and/or a fully diffuse medium, the cross-correlation function (CCF) should yield the true Green's function of the medium (Weaver & Lobkis, 2001; Fichtner & Tsai, 2019). However, such conditions are rarely fulfilled on Earth as the ambient seismic field is primarily generated by ocean waves at long periods (> 1 s) and by human activities at short periods.

Station-to-station CCFs are generally calculated over short ambient seismic field time windows ranging from a few minutes to hours, and are then stacked over a longer time period to increase their signal-to-noise ratios (SNRs). In addition to stacking, pre-processing of ambient seismic field records, such as 1-bit normalization and/or pre-whitening, is usually applied to improve the retrieval of the phase information of the CCFs (Bensen et al., 2007). The phase information of pre-processed CCFs has been extensively used to image the Earth's subsurface (Lin et al., 2008; Shapiro et al., 2005) and to monitor temporal changes occurring in the Earth through time (Brenguier, Campillo, et al., 2008; Brenguier, Shapiro, et al., 2008). However, the pre-processing steps generally involve non-linear operations which can bias the amplitude information of the CCFs.

Empirical studies showed that seismic interferometry by deconvolution with no pre-processing can be used to retrieve both the amplitude and phase information of CCFs (Viens et al., 2017). Deconvolution functions (DFs) have been used to simulate the long-period ground motions from moderate (Denolle et al., 2013; Prieto & Beroza, 2008; Sheng et al., 2017; Viens et al., 2014; Viens, Koketsu, et al., 2016) and large (Denolle et al., 2014, 2018; Viens, Miyake, & Koketsu, 2016) crustal earthquakes as well as mine collapse events (Kwak et al., 2017). However, the retrieval of reliable amplitudes is still debated as it strongly depends on the location and characteristics of ambient seismic field sources (Stehly et al., 2006; Stehly & Boué, 2017; Tsai, 2011).

The recent release of continuous data recorded by ocean bottom seismometers deployed on top of subduction zones worldwide offers new opportunities to better understand the complex seismic wave propagation through accretionary wedges. However, the retrieval of unbiased DFs between offshore and onshore stations is challenging as the ocean bottom environment is generally noisier than continental sites (Webb, 1998). Moreover, localized ambient seismic field sources between the two stations, such as ocean storms, can corrupt the DFs with spurious arrivals (Shapiro et al., 2006; Retailleau et al., 2017). Along the Nankai Trough, Japan, offshore-onshore DFs have been calculated and used to successfully simulate the long-period ground motions from moderate (Viens et al., 2015) and large (Viens & Denolle, 2019) subduction earthquakes. Nevertheless, the computed DFs are noisier than that retrieved between onshore station pairs and tend to contain spurious arrivals.

To improve the recovery of offshore-onshore DFs, we propose to use a two-step method based on unsupervised learning. For a pre-stack DF dataset calculated from short ambient seismic field time windows (e.g., a few minutes to hours) over a long period of time (e.g., one year) between two seismic stations, we first compute its Principal Component Analysis (PCA). We only keep the output of the first n principle components (PCs, with n being less than 20), which allows us to significantly reduce the dimensions of the dataset. Second, we cluster the data from the low-dimensional space and linearly stack the DFs belonging to each cluster together. Such a two-step method has been used to cluster different types of high-dimensional datasets, such as DNA gene expression and internet newsgroups (Ding & He, 2004). In seismology, a similar approach using dimensionality reduction with autoencoders and clustering has been developed to classify earthquake waveforms (Mousavi et al., 2019).

In this study, we first present our two-step clustering method and apply it to a synthetic dataset. We then introduce the computation of offshore-onshore DFs between seismic stations located on top and in the vicinity of the Nankai Trough. To validate the results from our method, we finally transform the DFs into velocity waveforms and compare them to the long-period (4–10 s) velocity waveforms from a moderate M_w 5.8 subduction earthquake, which occurred in the vicinity of an offshore station.

2 Methods: two-step clustering and application to a synthetic dataset

Clustering is a machine learning method that is used to partition a dataset into different groups with similar characteristics in an unsupervised manner. While clustering algorithms, such as k-means and Gaussian mixture models (GMMs), perform well on low dimensional datasets, their performance rapidly decreases as the dimension of the data increases (Steinbach et al., 2004). In seismic interferometry, thousands of DFs with a duration of a few hundred seconds can be computed from one year of continuous data recorded by a station pair, resulting in high-dimensional datasets.

2.1 PCA and clustering with Gaussian mixture model (GMM)

The PCA is a popular statistical approach to reduce the number of dimensions of a large dataset into a low-dimensional set of features. This is achieved by transforming the input data into a set of uncorrelated, orthogonal, principal components (PCs). The PCs are ordered so that the first PC explains the largest data variance, the second PC retains the second largest variance, etc. For more details about the PCA, we refer the reader to the extensively literature about the method (Jolliffe, 2002, and references therein).

In this study, our goal is to reduce the dimension of pre-stack DF datasets, which are calculated from short ambient seismic field time windows (e.g., 30 minutes) recorded over one year by station pairs (more details about the computation of the DFs are given in Section 3.1). For each DF dataset, we compute its PCA of and keep the output of the first n PCs. For offshore-onshore DFs, we keep the first 10 PCs (e.g., $n = 10$) and discuss our choice in the supplementary material Text S1 and Table S1. The data from the low-dimensional space of the n PCs are then clustered using a GMM. This probabilistic model clusters the data by assuming that they are generated from a mixture of a finite number of Gaussian distributions with unknown parameters. To learn the parameters of each Gaussian distribution, we use the expectation-maximization (EM) algorithm (Dempster et al., 1977).

One of the main problems of clustering algorithms is that the number of clusters needs to be accurately determined in advance to reduce potential under- or over-fitting of the data (Figueiredo & Jain, 2002). To automatically determine the optimal cluster number for a given DF dataset, we cluster the output of its first n PCs using GMMs with different numbers of clusters and compute the Bayesian Information Criterion (BIC, Schwarz, 1978) of each model. The optimal model is generally selected as the one with the lowest BIC score. Note that the formulation of the BIC considers a trade-off between model fitting and model complexity, with a penalty term to penalize more complex models which are most likely to better fit the data.

As stated above, the optimal number of clusters is generally identified with the minimum BIC value. However, it has been argued that the location of a knee (also called kink or elbow) in a BIC versus cluster number plot represents better the optimal number of clusters (Murphy, 2012; Zhao et al., 2008). While several methods have been developed to determine the knee location in BIC curves, we use that from Satopaa et al. (2011), which is based on the mathematical definition of curvature for a continuous function. For all the DF datasets considered in this study, the optimal number of clusters ranges between 2 and 6.

GMM clustering is performed on the output of the first n PCs using the optimal number of clusters and the DFs belonging to each cluster are linearly stacked together. Finally, one only needs to select the stacked DF that minimizes spurious arrivals and maximizes the symmetry between the anti-causal (negative) and causal (positive) parts among the 2 to 6 stacked DFs. We provide more information about the automatic selection of the best DF in

Section 3.2. The main advantage of using unsupervised learning to improve the retrieval of DFs is that no metric is required to select the waveforms which need to be stacked together. Moreover, applying this method to a DF dataset with thousands of waveforms is fast and can easily be used as an additional step when processing ambient seismic field time series.

2.2 Synthetic dataset

We first apply our method to a simple synthetic dataset to test its performance on waveforms with known signal and noise properties. We consider the propagation of surface waves between two hypothetical stations (A and B). To reproduce the dispersive property of surface waves, we use a chirp function with initial and final frequencies of 0.05 and 0.25 Hz, respectively. The duration of the chirp signal is 70 s and starts at a lag-time of 10 s. The amplitude of the chirp signal is constant through time with a value of 0.5 and both ends of the signal are slightly tapered. The sampling rate of the waveforms is 2 Hz. In this synthetic example, we do not intend to replicate real correlation functions from the ambient seismic field, which is complicated to simulate due to its different of source mechanisms and the complex wave propagation through the Earth.

To mimic a correlation function dataset that could be biased by an uneven distribution of noise sources, we construct 10,000 waveforms with four different types of signals. The first 2,000 waveforms represent correlation functions obtained with a uniform distribution of the noise sources around the two stations. Therefore, both the anti-causal and causal parts of the CCFs can be retrieved (Figure 1a, top gray waveform). The next 2,000 waveforms (waveform number 2,001 to 4,000) represent the case where noise sources are still uniformly distributed around the two stations, but local noise sources (e.g., ocean storms) are also active between the station pair. This leads to clear spurious arrivals in addition to the anti-causal and causal signals. The spurious arrivals are created using a 0.11 Hz cosine function with a higher amplitude than the chirp signal. From waveform number 4,001 to 6,000, we consider the case where noise sources are located between the two stations and in the stationary phase zone of station B. Therefore, the CCFs only contain the anti-causal part of the signal (e.g., propagation from station B to station A) as well as spurious arrivals. The last of the four groups is composed of 4,000 waveforms with no signal. We then add some random noise drawn from Gaussian distributions with a mean of zero and a variance of 1 to all the waveforms. Note that the random noise values are normalized so the maximum absolute noise value is equal to 1.0, which corresponds to twice the maximum amplitude of the chirp signal, before being added to the waveforms (Figure 1a, background color and black waveforms). Finally, we randomly shuffle the 10,000 noisy waveforms and show them in Figure 1b. The raw stack of all the waveforms cancels the random noise but strong spurious arrivals can be observed and the anti-causal and causal signals have different amplitudes (Figure 1b, gray waveform).

2.3 Clustering the synthetic waveforms

The PCA of the shuffled dataset is calculated and its projection on the first two PCs is shown in Figure 2a. For this synthetic example, we only keep the output of the first 2 PCs, which explain 20.4% of the cumulative data variance. This value is very close to the 23.4% cumulative data variance explained by the first 10 PCs. This can be explained by the fact that all waveforms in this synthetic example are constructed with similar chirp and cosine signals to which white noise is added. Therefore, the chirp and cosine signals are defined by the first 2 PCs and the white noise by the following PCs. Note that for real offshore-onshore DF datasets, the output of more PCs is required due to the complexity of the waveforms.

To determine the appropriate number of clusters for the GMM, we cluster the output of the first 2 PCs using GMMs with 2 to 15 clusters and compute the BIC of each model (Figure 2b). We then use the knee method to determine that the optimal number of clusters is four (red dot in Figure 2b). For this synthetic case, the lowest value of the BIC corresponds to the optimal number of clusters. The clustering performed with the GMM using four clusters is represented by the colors in Figure 2a. We finally stack the waveforms belonging to each cluster and show them in Figure 2c. In this example, the four types of noisy waveforms are clustered with an accuracy of 100%, meaning that no waveform is miss-classified. The linear stack of the data from each group cancels the random noise and allows us to retrieve the four types of initial signals. As the goal of seismic interferometry is to retrieve unbiased correlation functions with no spurious arrivals to infer the physical properties of the Earth, one only needs to select the waveform from cluster 3 in this synthetic example. Note that the cluster number might change if the clustering is performed multiple times.

3 Application to real offshore-onshore deconvolution functions

3.1 Computation of deconvolution functions

We focus on one year of continuous data recorded by the KME18 DONET sensor and 77 high-sensitivity Hi-net seismometers from April 1, 2015 to March 31, 2016. All the stations in this study record with a sampling rate of 100 Hz and are shown in Figure 3. The raw data are first corrected for their instrument responses, down-sampled to 4 Hz to speed up the computation process, and band-pass filtered between 1 and 20 s using a 2-pass 4-pole Butterworth filter. As the KME18 virtual source and the 77 Hi-net receivers are buried in boreholes with depths ranging from 1 m to 3000 m, we rotate the two horizontal components of each station to the true north-south (N) and east-west (E) directions using the orientations determined by Nakano et al. (2012) and Shiomi (2013). We then divide the dataset into 30-min-long time series and discard windows with spikes larger than 10 times the standard deviation of the window to remove the effect of potential earthquakes. We finally compute the deconvolution functions between offshore and onshore stations as

$$\mathrm{DF}_{i,j}(x_r, x_s, t) = F^{-1}\left(\frac{\hat{v}_i(x_r,\omega)\hat{v}_j^*(x_s,\omega)}{\{|\hat{v}_j(x_s,\omega)|\}^2}\right), \qquad (1)$$

where $\hat{v}_j^*(x_s,\omega)$ and $\hat{v}_i^*(x_r,\omega)$ are the Fourier transforms of a 30-min long velocity record at the offshore virtual source (x_s) and the onshore receiver (x_r) for the jth and ith components (either N, E, or vertical Z). ω represents the frequency domain, the * symbol denotes the complex conjugate, $|\cdot|$ is the absolute value, and $\{\cdot\}$ represents a smoothing of the spectrum using a 20-point moving average to stabilize the denominator term. The inverse Fourier transform (F^{-1}) is applied to retrieve the DFs between the two stations in the time domain (denoted by t). We taper the first and last 1.5 s of the anti-causal (negative) and causal (positive) parts of each DF with a 6-point half-Hanning function. DFs are then time derived once to retrieve the proportionality between the correlation function and the Green's function, and the causal part is multiplied by -1 to retrieve the symmetry between the anti-causal and causal parts. For each station pair, we then rotate the 9-component DF tensor from the east-north-vertical (ENZ) coordinate system to the radial-transverse-vertical (RTZ) system, where R and T are the radial and transverse directions from the virtual source, respectively. In the following, we assume that Love waves are retrieved on the T–T DFs and that Rayleigh waves are captured by the Z–Z and R–R DFs. Finally, all the waveforms are band-pass filtered between 4 and 10 s using a 2-pass 4-pole Butterworth filter.

We show an example of the DFs calculated between the KME18 and ABNH stations every 30-min for the Z–Z component in Figure 4. For this station pair, we obtain a total number of 16,641 waveforms, which is less than the total number of waveforms over 366 days (e.g, 17,568 waveforms) as some time windows are removed during the pre-processing step. In Figure 4a, we show the raw stack of the offshore-onshore 30-min DFs over the year. Assuming a theoretical surface wave velocity of 3.5 km/s, the first physical signals should arrive after 45 s given the 159 km inter-station distance. Therefore, the clear arrivals in the anti-causal part between -50 s and -130 s, which are barely visible on the causal part, are likely Rayleigh waves propagating between the two stations. However, the strongest signal which dominates the waveform in Figure 4a arrives near the zero-lag time. Such non-physical arrivals are likely generated by ambient seismic field sources located between the two stations, as the inter-station path is mainly under the ocean (station locations in

Figure 3). Finally, we can observe in Figure 4b that the amplitude of the spurious arrivals varies through the year and is the strongest for the DFs calculated from the data recorded between April and June 2015.

3.2 Clustering offshore-onshore deconvolution functions

We apply the two-step clustering method to the 16,641 Z–Z DFs between the KME18 and ABNH stations and show the results in Figure 5. We first compute the PCA of the dataset and keep the output of the first 10 PCs, which explain 22.5% of the cumulative data variance. Similarly to the synthetic data, we cluster the output of the first 10 PCs using GMMs with 2 to 15 clusters and compute the BIC of each model (Figure 5b). We then use the knee method to determine that the optimal number of clusters is four. Note that contrary to the synthetic example, the BIC value for four clusters is slightly higher than the minimum BIC value, which is found for six clusters. The projection of the data on the first two PCs is shown in Figure 5a together with the clustering results. We only present the projection of the data on the first two PCs as visualizing the data over 10 dimensions is impossible. Unlike the synthetic case, no clear clusters can be observed in the plot of the first two PCs nor in other PC combinations. Nevertheless, the waveforms obtained from the stack of the DFs from each cluster have different characteristics (Figure 5c).

In Figure 5c, the stacked DF from the fourth cluster is very similar to the raw stack over the year and contains strong spurious arrivals as well as Rayleigh wave arrivals in its anti-causal and causal parts. The waveform from the first cluster is also very similar, but does not contain any Rayleigh wave arrivals in its causal part. The stacked DF from the second cluster contains clear Rayleigh wave arrivals in its anti-causal and causal parts, but still contains strong spurious arrivals. Finally, the waveform from the third cluster, which is made by the stack of 1,973 30-min DFs, does not contain any spurious arrivals and has clear anti-causal and causal arrivals with almost similar amplitudes. As our goal is to improve the retrieval of offshore-onshore DFs, we select the waveform from cluster 3 for the Z–Z component between the KME18 and ABNH stations.

To automate the selection of the best stacked DF, we use the fact that the data of the corresponding cluster lay near the origin of the first 2-PC plot and have the lowest variance. This property is consistent for all the stations and all components of the Green's tensor, and can be observed in Figure 5a for the data from the third cluster. Therefore, we simply compute the variance of the data from each cluster on the first 2 PCs and automatically select the stacked DF from the cluster with the lowest variance in the following.

We show the DFs between the KME18 station and the 77 onshore Hi-net stations for the T–T, R–R, and Z–Z components calculated with the raw stack over the year in Figure 6a, and with the two-step clustering method in Figure 6b. In the 4 to 10 s period range, spurious arrivals can be observed for the three components of the raw stack DFs, and are especially strong for the Z–Z component (Figure 6a). The two-step clustering method allows us to remove the spurious arrivals from the DFs. To quantify the effect of our method on the retrieval of clear DFs, we compute a SNR value for each component (e.g., T–T, R–R, and Z–Z) in three steps. First, we compute the ratio of the peak amplitude of the waves traveling slower than 3.5 km/s over the standard deviation of the first 25 s for both the anti-causal and causal parts of each DF. Second, we compute the mean of the anti-causal and causal SNR values for each DF. Finally, we average the SNR values for each component over 76 Hi-net stations to obtain one SNR value per component and shown them in each panel of Figure 6. We exclude the station located at less than 75 km from the virtual source as the first physical wave arrivals are likely to be in the first 25 s of the signal. For the three components, the SNRs of the DFs calculated with our method are higher than that from the DFs obtained with the raw stack over the year. Note that the SNR values are also used to determine the number of PCs that are needed to retrieve the best DFs (Supplementary material Text S1 and Table S1).

To investigate the mechanisms involved in the retrieval of clear DFs with the two-step clustering method between the KME18 virtual source and the 77 onshore Hi-net stations, we show the daily number of selected DFs averaged over all the receiver stations between April 1, 2015 and March 31, 2016 in Figure 7. Between May and November 2015, there are five distinct time periods where the two-step clustering method selects approximately twenty 30-min DFs per day for the three components. Extreme meteorological events, such as storms, typhoons, and cyclones, are well known to efficiently excite the ambient seismic field and to favor the retrieval of correlation functions (Nishida, 2017, and references therein). To determine if the DF selection can be explained by the effect of storms, we compute a metric using the typhoon data gathered by the Japan Meteorological Agency (JMA). First, we select the 14 severe tropical storms (wind speed between 89 and 117 km/h), typhoons (wind speed $\geq$ 118 km/h), and extra-tropical cyclones passing at less than 1,500 km from the virtual source. Second, we compute the metric by multiplying the sea level atmospheric pressure at the center of each storm by its distance to the virtual source (Figure 7). We find a positive correlation between the computed metric and the daily number of selected DFs over the considered time period, with correlation coefficients of 0.61, 0.58, and 0.68 for the T–T, R–R, and Z–Z components, respectively. This indicates that severe meteorological events occurring near the region of interest efficiently excite the ambient seismic field in a way that favors the retrieval of clear offshore-onshore DFs. In 2016, however, the 30-min DFs selected by the two-step clustering method cannot be explained by typhoons. Takagi et al. (2018) showed that Rayleigh waves in the 4 to 8 s period range are mainly generated in the Japan Sea (also known as East Sea) during winter months. Therefore, the selection of DFs in 2016 can potentially be caused by the occurrence of storms in the Japan Sea. However, additional work outside the scope of this study is required to fully understand the mechanisms contributing to the retrieval of better offshore-onshore DFs.

3.3 Moderate earthquake simulation

3.3.1 Earthquake data

A M_{w} 5.8 earthquake occurred on April 1, 2016 at 11:39:07 Japan Standard Time in the vicinity of the KME18 station (Figure 3). The F-net solution of the National Research Institute for Earth Science and Disaster Resilience (NIED) locates the earthquake at a depth of 12 km, which is close to the plate interface, with a subduction dominant focal mechanism. The occurrence of the earthquake on the plate interface was later confirmed by further studies (Wallace et al., 2016; Nakano et al., 2018; Takemura et al., 2018). We correct the earthquake velocity records at the 77 Hi-net stations for their instrument responses and rotate the horizontal waveforms to the radial and transverse directions from the epicenter. The three-component velocity data are then band-pass filtered between 4 and 10 s using a four-pole and two-pass Butterworth filter and are down-sampled from 100 Hz to 10 Hz.

3.3.2 Simulating velocity waveforms with DFs

To demonstrate that the DFs obtained with our two-step clustering method have reliable phases and amplitudes, we use them to simulate the velocity waveforms from the M_{w} 5.8 earthquake, which can be considered as a point source for the period range of interest (e.g., 4–10 s). Similarly to Viens and Denolle (2019), we consider the causal part of the T–T, R–R, and Z–Z DFs as it likely better captures the site amplification and attenuation effects compared to the anti-causal part (Bowden et al., 2015; Liu et al., 2016). In the following, the causal T–T DFs are considered to simulate Love waves (e.g., T component from the earthquake) and the causal R–R and Z–Z DFs are used to simulate Rayleigh waves, which are the R and Z components from the earthquake.

We first resample the causal part of the DFs from 4 Hz to 10 Hz and convolve them with a source time function to simulate velocity waveforms. The source time function is a Gaussian function with a duration of 1 s and its amplitude is set so its integral over its duration is equal to 4.9×10^{17} Nm, which is the seismic moment of the earthquake determined by the F-net NIED solution. To account for the fact that the earthquake epicenter is located 7 km away from the KME18 station, we multiply the amplitude of the simulated waveform by the difference of surface-wave geometrical spreading (e.g., multiplication by $\sqrt{d_{v-r}}/\sqrt{d_{e-r}}$, with d_{v-r} and d_{e-r} being the KME18-receiver and epicenter-receiver distances, respectively). We also time shift the simulated waveforms considering a constant local surface-wave velocity of 3.0 km/s, assuming that surface-wave dispersion is negligible in the 4 to 10 s period range. Finally, as only the relative, rather than absolute, amplitude is preserved by the DFs, the simulated velocity waveforms need to be calibrated with the velocity waveforms from the earthquake. We compute a calibration factor common to the 77 Hi-net stations but different for each component by taking average of the ratio of the simulated over recorded surface-wave long-period peak ground velocity (PGV) over all stations. The surface-wave long-period PGV of each waveform is defined as the maximum absolute amplitude of the waves traveling slower than 3.5 km/s.

Surface-wave radiation pattern effects should also be taken into account when simulating earthquakes with DFs (Denolle et al., 2013). However, Viens and Denolle (2019) showed that for a M_{w} 5.5 event which occurred near the trench in the Tonankai region, the effect of the seismic wave propagation through the accretionary wedge is stronger than radiation pattern effects. To demonstrate that a similar effect can be observed for the M_{w} 5.8 earthquake, we correct the simulated and observed velocity waveforms for the surface wave geometrical spreading effect by multiplying the waveforms by $\sqrt{d_{e-r}}$. The observed and simulated surface-wave long-period PGV after geometrical spreading correction are shown in Figure 8 as a function of the azimuth from the epicenter. Similar long-period PGV variations with the azimuth can be observed for the three components. For the observed radial (R) and vertical (Z) components and the simulated waveforms with R–R and Z–Z components, the amplitude of the long-period PGVs decreases with increasing azimuth. For the recorded transverse (T) and simulated with T–T components, a peak of maximum PGV values can be observed around the zero azimuth and minimum values are located near the -30 and 30 degree azimuths. As the simulated waveforms only contain the signature of the seismic wave propagation between the KME18 station and onshore stations, similar azimuthal variations as the earthquake suggest that propagation effects have a dominant effect on the amplitude of the seismic waves, and are stronger than radiation pattern effects for the M_{w} 5.8 earthquake in the 4 to 10 s period range.

Therefore, we simply consider the causal T–T, R–R, and Z-Z DFs convolved with the source time function and corrected for the fact that the KME18 station and the epicenter are not co-located to simulate the transverse, radial, and vertical earthquake waveforms. In the following, we consider two types of simulated waveforms. The first type of simulations uses the raw stack of the DFs over the year, which are call raw simulations, and the second type of simulated waveforms uses the DFs obtained with the two-step clustering method, which are called clustered simulations.

3.3.3 Simulation results

In Figure 9, we show the simulated and observed velocity waveforms for the transverse, radial, and vertical components at six Hi-net stations (location in Figure 3). The raw and clustered simulations are shown in Figure 9a and Figure 9b, respectively. For the three components, the main wave packet travels with a velocity of 3.5 km/s and is relatively well retrieved by the two simulation methods. However, the clustered simulations have less spurious arrivals, which allows us to better identify the true wave arrivals.

To quantitatively compare the observed and simulated waveforms, we compute a correlation coefficient (CC) for each waveform pair. The correlation coefficient is calculated over 100 s from the time 1% of the earthquake cumulative energy is reached. This metric varies between -1, when the two waveforms are out of phase by 180 degree, to 1 when the two waveforms are identical. Note that we allow a 1 s phase shift when calculating CCs to account for potential errors of the earthquake location. For the 6 stations shown in Figure 9, the clustered simulations generally reproduce better the phase of the earthquake waveforms, as shown by the higher CCs for 12 of the 18 waveform pairs. Over the 231 waveforms compared in this study (e.g., 77 receiver stations and 3 components), 152 CCs (e.g., 66%) calculated between the observed waveforms and clustered simulations are higher or equal than if the raw simulations are used. For the 79 smaller CCs, 68 of them are smaller by less than a value of 0.1, which indicates that the raw and clustered simulations are very similar (e.g., T and R components of the TAGH station in Figure 9).

To quantify the difference between the observed and simulated waveform amplitudes, we use the surface-wave long-period PGVs and compute their residuals as the natural logarithm of the simulated over observed PGV ratios. The residuals are shown in Figure 10 as a function of the distance to the earthquake epicenter. For both types of simulated waveforms, the mean of the residuals is close to the zero-bias. Moreover, there is no clear variation of the residual distribution with the distance to the epicenter in Figure 10. This indicates that the attenuation of the waves with distance is relatively well preserved by both the raw stack and clustered DFs. However, the PGVs from the clustered simulations (Figure 10b) reproduce better the observed PGVs as shown by the smaller standard deviations to the mean for the three components, compared to that shown in Figure 10a for the PGVs from the raw simulations. Note that 223 out of the 231 PGV ratios between the clustered simulations and observed waveforms are smaller than a factor of two, and the 8 other ratios are larger than a factor of two but smaller than a factor of three (green and blue circles in Figure 10b). For the raw simulations, 218 PGV ratios are within a factor of two, one ratio is larger than 3, and the other 12 ratios are larger than a factor of two but smaller than a factor of three.

We finally compute the 5% damped spectral acceleration (SA) for the observed and simulated velocity waveforms. First, velocity waveforms are time derived once to retrieve the corresponding acceleration time series and the SA is calculated using the Duhamel's integral technique (Chopra, 2015). We then compute the SA residuals as the natural logarithm of the simulated over observed SAs for each period. Finally, we calculate the mean of the residuals over the 77 stations as well as the one and two standard deviations to the mean for each period and show the results in Figure 11. For the radial and vertical components, the clustered simulations perform better than the raw simulations as the mean of the SA residuals is closer to the zero bias and the standard deviation values at each periods are smaller. Moreover, the zero-bias line in Figure 11b is always within one standard deviation, which is not the case for the vertical component in Figure 11a. For the transverse component, the SA residuals are not as good as for the radial and vertical components for both simulation methods. Nevertheless, the clustered simulations perform better than the raw simulations to simulate the SA from the recorded earthquake. The variations observed for the transverse component can potentially be caused by the fact that Love waves are not as well retrieved as Rayleigh waves in the offshore-onshore setting. This can be observed in Figure 6 with the raw and clustered T–T DFs have the lowest SNR values among the three components.

4 Conclusions

We introduced a method based on unsupervised learning to improve the retrieval of offshore-onshore correlation functions calculated with the deconvolution technique (DF). Our method works in two steps: first, the dimension of a DF dataset calculated between two seismic stations is reduced using the PCA; and second, the data from the low-dimensional space are clustered with a Gaussian mixture model. The waveforms belonging to each cluster are finally stacked together and the clustered DF that improves the symmetry between the anti-causal and causal parts and removes spurious arrivals is selected.

We applied our method to DFs calculated between the offshore KME18 station and 77 onshore Hi-net stations in Japan. The selected DFs clustered with our method have higher signal-to-noise ratios than that obtained with the raw stack of the DFs over the year. To demonstrate that the DFs calculated with the clustering method contain reliable phases and amplitudes, we transformed the DFs into velocity waveforms and compared them to the recorded waveforms of a M_{w} 5.8 earthquake, which occurred close to the virtual source.

The simulated waveforms obtained with the clustered DFs reproduced better the earthquake waveforms than the simulated waveforms calculated with the raw stack of the DFs over the year.

Our two-step clustering method offers a new way to easily improve the quality of correlation functions between offshore and onshore stations, without having to determine any metric to select the DFs that need to be stacked together. By improving the retrieval of reliable DFs between offshore and onshore stations, we hope to improve the prediction of long-period ground motions from potential future megathrust earthquakes that could occur along subduction zones worldwide, such as the Nankai Trough or the Cascadia subduction zone.

Acknowledgments

We thank Chris Van Houtte for useful discussions. The continuous data from the NIED Hi-net (`https://doi.org/10.17598/NIED.0003`) and DONET 1 (`https://doi.org/10.17598/NIED.0008`) networks can be downloaded at `http://www.hinet.bosai.go.jp`. The clustering algorithm developed in this study is available at `https://github.com/lviens` together with the codes to reproduce Figures 1, 2, 4, and 5. Most figures were made using the Matplotlib library (Hunter, 2007). LV is supported by the JSPS Postdoctoral Fellowship for Research in Japan award number P18108.

References

Bensen, G. D., Ritzwoller, M. H., Barmin, M. P., Levshin, A. L., Lin, F., Moschetti, M. P., . . . Yang, Y. (2007). Processing seismic ambient noise data to obtain reliable broadband surface wave dispersion measurements. *Geophys. J. Int.*, *169*, 1239–1260. doi: 10.1111/j.1365-246X.2007.03374.x

Bowden, D. C., Tsai, V. C., & Lin, F. C. (2015). Site amplification, attenuation, and scattering from noise correlation amplitudes across a dense array in Long Beach, CA. *Geophys. Res. Lett.*, *42*, 1360–1367. doi: 10.1002/2014GL062662

Brenguier, F., Campillo, M., Hadziioannou, C., Shapiro, N. M., Nadeau, R. M., & Larose, E. (2008). Postseismic relaxation along the San Andreas fault at Parkfield from continuous seismological observations. *Science*, *321*, 1478–1481. doi: 10.1126/science.1160943

Brenguier, F., Shapiro, N. M., Campillo, M., Ferrazzini, V., Duputel, Z., Coutant, O., & Nercessian, A. (2008). Towards forecasting volcanic eruptions using seismic noise. *Nature Geoscience*, *1*, 126–130. doi: 10.1038/ngeo104

Chopra, A. (2015). *Dynamics of structures: International edition.* Pearson Education Limited.

Dempster, A. P., Laird, N. M., & Rubin, D. B. (1977). Maximum likelihood from incomplete data via the em algorithm. *Journal of the royal statistical society, Series B*, *39*(1), 1–38.

Denolle, M. A., Boué, P., Hirata, N., & Beroza, G. C. (2018). Strong shaking predicted in tokyo from an expected m7+ itoigawa-shizuoka earthquake. *J. Geophys. Res. Solid Earth*, *123*, 3968-3992. doi: 10.1029/2017JB015184

Denolle, M. A., Dunham, E. M., Prieto, G. A., & Beroza, G. C. (2013). Ground motion prediction of realistic earthquake sources using the ambient seismic field. *J. Geophys. Res. Solid Earth*, *118*, 2102–2118. doi: 10.1029/2012JB009603

Denolle, M. A., Dunham, E. M., Prieto, G. A., & Beroza, G. C. (2014). Strong ground motion prediction using virtual earthquakes. *Science*, *343*, 399–403. doi: 10.1126/science.1245678

Ding, C., & He, X. (2004). K-means clustering via principal component analysis. In *Proceedings of the twenty-first international conference on machine learning* (pp. 29–). New York, NY, USA: ACM. doi: 10.1145/1015330.1015408

Fichtner, A., & Tsai, V. C. (2019). Theoretical foundations of noise interferometry. In N. Nakata, L. Gualtieri, & A. Fichtner (Eds.), *Seismic ambient noise.* Cambridge

University Press.
Figueiredo, M. A. T., & Jain, A. K. (2002, March). Unsupervised learning of finite mixture models. *IEEE Transactions on Pattern Analysis and Machine Intelligence*, *24*(3), 381-396. doi: 10.1109/34.990138
Hunter, J. D. (2007). Matplotlib: A 2d graphics environment. *Computing In Science & Engineering*, *9*(3), 90–95. doi: 10.1109/MCSE.2007.55
Jolliffe, I. (2002). *Principal component analysis.* Springer.
Kwak, S., Song, S. G., Kim, G., Cho, C., & Shin, J. S. (2017). Investigating the capability to extract impulse response functions from ambient seismic noise using a mine collapse event. *Geophys. Res. Lett.*, *44*, 9653–9662. doi: 10.1002/2017GL075532
Lin, F.-C., Moschetti, M. P., & Ritzwoller, M. H. (2008). Surface wave tomography of the western United States from ambient seismic noise: Rayleigh and Love wave phase velocity maps. *Geophys. J. Int.*, *173*, 281–298. doi: 10.1111/j.1365-246X.2008.03720.x
Liu, X., Ben-Zion, Y., & Zigone, D. (2016). Frequency domain analysis of errors in cross-correlations of ambient seismic noise. *Geophys. J. Int.*, *207*, 1630-1652. Retrieved from `http://dx.doi.org/10.1093/gji/ggw361` doi: 10.1093/gji/ggw361
Mousavi, S. M., Zhu, W., Ellsworth, W., & Beroza, G. (2019, Nov). Unsupervised clustering of seismic signals using deep convolutional autoencoders. *IEEE Geoscience and Remote Sensing Letters*, *16*(11), 1693-1697. doi: 10.1109/LGRS.2019.2909218
Murphy, K. P. (2012). *Machine learning : a probabilistic perspective.* Cambridge, Mass., USA: MIT Press.
Nakano, M., Hyodo, M., Nakanishi, A., Yamashita, M., Hori, T., Kamiya, S.-i., . . . Kaneda, Y. (2018). The 2016 mw 5.9 earthquake off the southeastern coast of mie prefecture as an indicator of preparatory processes of the next nankai trough megathrust earthquake. *Progress in Earth and Planetary Science*, *5*, 30. doi: 10.1186/s40645-018-0188-3
Nakano, M., Tonegawa, T., & Y., K. (2012). Orientations of donet seismometers estimated from seismic waveforms. *JAMSTEC Rep. Res. Dev.*, *15*, 77-89.
Nishida, K. (2017). Ambient seismic wave field. *Proceedings of the Japan Academy. Series B, Physical and biological sciences*, *93*, 423–448. doi: 10.2183/pjab.93.026
Prieto, G. A., & Beroza, G. C. (2008). Earthquake ground motion prediction using the ambient seismic field. *Geophys. Res. Lett.*, *35*, L14304. doi: 10.1029/2008GL034428
Retailleau, L., Boué, P., Stehly, L., & Campillo, M. (2017). Locating microseism sources using spurious arrivals in intercontinental noise correlations. *J. Geophys. Res. Solid Earth*, *122*, 8107-8120. doi: 10.1002/2017JB014593
Satopaa, V., Albrecht, J., Irwin, D., & Raghavan, B. (2011, June). Finding a "kneedle" in a haystack: Detecting knee points in system behavior. In *2011 31st international conference on distributed computing systems workshops* (p. 166-171). doi: 10.1109/ICDCSW.2011.20
Schwarz, G. (1978, 03). Estimating the dimension of a model. *Ann. Statist.*, *6*, 461–464. doi: 10.1214/aos/1176344136
Shapiro, N. M., Campillo, M., Stehly, L., & Ritzwoller, M. H. (2005, 11). High-resolution surface-wave tomography from ambient seismic noise. *Science*, *307*, 1615–1618. doi: 10.1126/science.1108339
Shapiro, N. M., Ritzwoller, M. H., & Bensen, G. D. (2006). Source location of the 26 sec microseism from cross-correlations of ambient seismic noise. *Geophys. Res. Lett.*, *33*, L18310. doi: 10.1029/2006GL027010
Sheng, Y., Denolle, M. A., & Beroza, G. C. (2017). Multicomponent c3 green's functions for improved longperiod groundmotion prediction. *Bull. Seismol. Soc. Am.*, *107*, 2836. doi: 10.1785/0120170053
Shiomi, K. (2013). New measurements of sensor orientation at nied hi-net stations. *Report NIED*, *80*, 1–20.
Stehly, L., & Boué, P. (2017). On the interpretation of the amplitude decay of noise correlations computed along a line of receivers. *Geophys. J. Int.*, *209*, 358. doi: 10.1093/gji/ggx021

Stehly, L., Campillo, M., & Shapiro, N. M. (2006). A study of the seismic noise from its long-range correlation properties. *J. Geophys. Res. Solid Earth*, *111*, B10306. doi: 10.1029/2005JB004237

Steinbach, M., Ertöz, L., & Kumar, V. (2004). The challenges of clustering high dimensional data. In L. T. Wille (Ed.), *New directions in statistical physics: Econophysics, bioinformatics, and pattern recognition* (pp. 273–309). Berlin, Heidelberg: Springer Berlin Heidelberg. doi: 10.1007/978-3-662-08968-2_16

Takagi, R., Nishida, K., Maeda, T., & Obara, K. (2018). Ambient seismic noise wavefield in japan characterized by polarization analysis of hi-net records. *Geophys. J. Int.*, *215*, 1682-1699. doi: 10.1093/gji/ggy334

Takemura, S., Kimura, T., Saito, T., Kubo, H., & Shiomi, K. (2018). Moment tensor inversion of the 2016 southeast offshore mie earthquake in the tonankai region using a three-dimensional velocity structure model: effects of the accretionary prism and subducting oceanic plate. *Earth Planets Space*, *70*, 50. doi: 10.1186/s40623-018-0819-3

Tsai, V. C. (2011). Understanding the amplitudes of noise correlation measurements. *J. Geophys. Res. Solid Earth*, *116*, B09311. doi: 10.1029/2011JB008483

Viens, L., Denolle, M., Miyake, H., Sakai, S., & Nakagawa, S. (2017). Retrieving impulse response function amplitudes from the ambient seismic field. *Geophys. J. Int.*, *210*, 210. doi: 10.1093/gji/ggx155

Viens, L., & Denolle, M. A. (2019). Long-Period Ground Motions from Past and Virtual Megathrust Earthquakes along the Nankai Trough, Japan. *Bull. Seismol. Soc. Am.*, *109*, 1312-1330. doi: 10.1785/0120180320

Viens, L., Koketsu, K., Miyake, H., Sakai, S., & Nakagawa, S. (2016). Basin-scale Green's functions from the ambient seismic field recorded by MeSO-net stations. *J. Geophys. Res. Solid Earth*, *121*, 2507–2520. doi: 10.1002/2016JB012796

Viens, L., Laurendeau, A., Bonilla, L. F., & Shapiro, N. M. (2014). Broad-band acceleration time histories synthesis by coupling low-frequency ambient seismic field and high-frequency stochastic modelling. *Geophys. J. Int.*, *199*, 1784–1797. doi: 10.1093/gji/ggu362

Viens, L., Miyake, H., & Koketsu, K. (2015). Long-period ground motion simulation of a subduction earthquake using the offshore-onshore ambient seismic field. *Geophys. Res. Lett.*, *42*, 5282–5289. doi: 10.1002/2015GL064265

Viens, L., Miyake, H., & Koketsu, K. (2016). Simulations of long-period ground motions from a large earthquake using finite rupture modeling and the ambient seismic field. *J. Geophys. Res. Solid Earth*, *121*, 2507–2520. doi: 10.1002/2016JB012796

Wallace, L. M., Araki, E., Saffer, D., Wang, X., Roesner, A., Kopf, A., … Carr, S. (2016). Near-field observations of an offshore mw 6.0 earthquake from an integrated seafloor and subseafloor monitoring network at the nankai trough, southwest japan. *J. Geophys. Res. Solid Earth*, *121*, 8338-8351. doi: 10.1002/2016JB013417

Weaver, R. L., & Lobkis, O. I. (2001, Sep). Ultrasonics without a Source: Thermal Fluctuation Correlations at MHz Frequencies. *Phys. Rev. Lett.*, *87*, 134301. doi: 10.1103/PhysRevLett.87.134301

Webb, S. C. (1998). Broadband seismology and noise under the ocean. *Reviews of Geophysics*, *36*, 105-142. doi: 10.1029/97RG02287

Zhao, Q., Hautamaki, V., & Fränti, P. (2008). Knee point detection in bic for detecting the number of clusters. In J. Blanc-Talon, S. Bourennane, W. Philips, D. Popescu, & P. Scheunders (Eds.), *Advanced concepts for intelligent vision systems* (pp. 664–673). Berlin, Heidelberg: Springer Berlin Heidelberg.

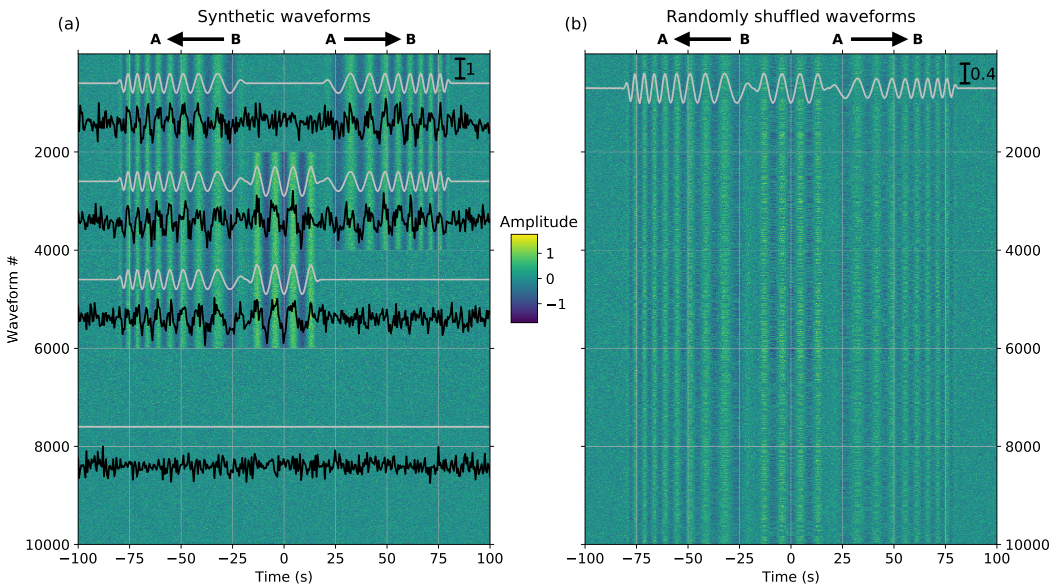

Figure 1. (a) Synthetic waveforms propagating from station A to station B (positive part) and from station B to station A (negative part). For the four different types of waveforms, an example of the clean and noisy traces are shown in gray and black, respectively. The background color represents the noisy waveforms. (b) Randomly shuffled waveforms. The gray trace represents the raw stack of the 10,000 waveforms. The amplitude scale of the gray waveform in the top right-hand corner is different than that in (a).

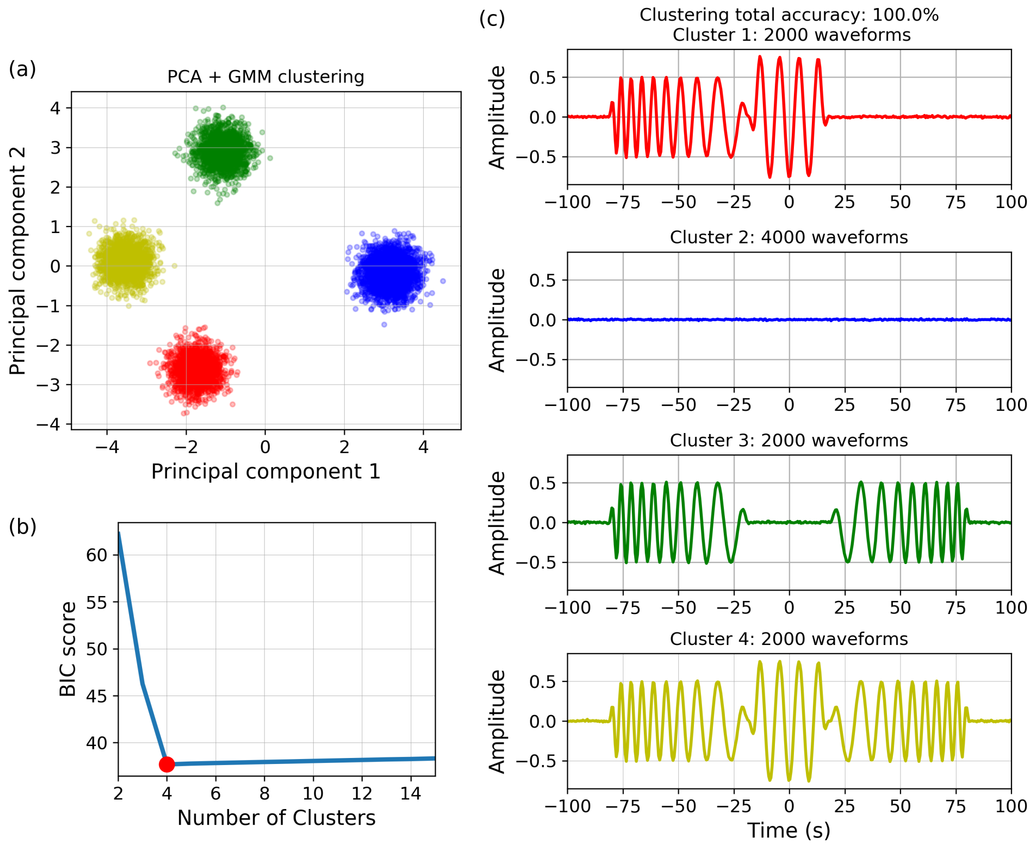

Figure 2. (a) Projection of the synthetic data on the first two principal components of the PCA. The four colors correspond to the four clusters obtained with the Gaussian mixture model (GMM). (b) BIC score for GMMs performed on the output of the first two PCs with different numbers of clusters. The lowest and optimal BIC value obtained with the knee method is found for four clusters. (c) Stack of the waveforms from each cluster. The random noise added to the data is canceled by the stacking of the waveforms and the four types of waveforms originally created are retrieved. The total accuracy of the clustering is also indicated on top of (c) and is 100% for this synthetic example.

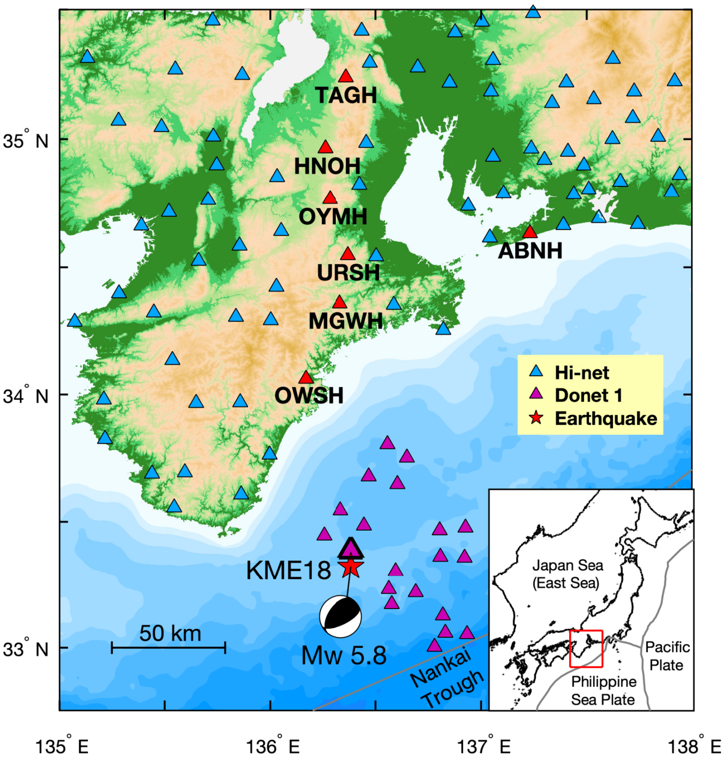

Figure 3. Topographic map of the region of interest, including the 20 offshore DONET 1 (purple) stations and the 77 onshore Hi-net (blue) receivers. The location of the 2016 M_{w} 5.8 earthquake, which occurred 7 km away from the KME18 station, is shown by the red star with its focal mechanism. The seven Hi-net stations used in this study are highlighted by red triangles and their names are also indicated. The inset map shows the Japan Islands, the plate boundaries (gray lines), and the location of the region of interest (red rectangle).

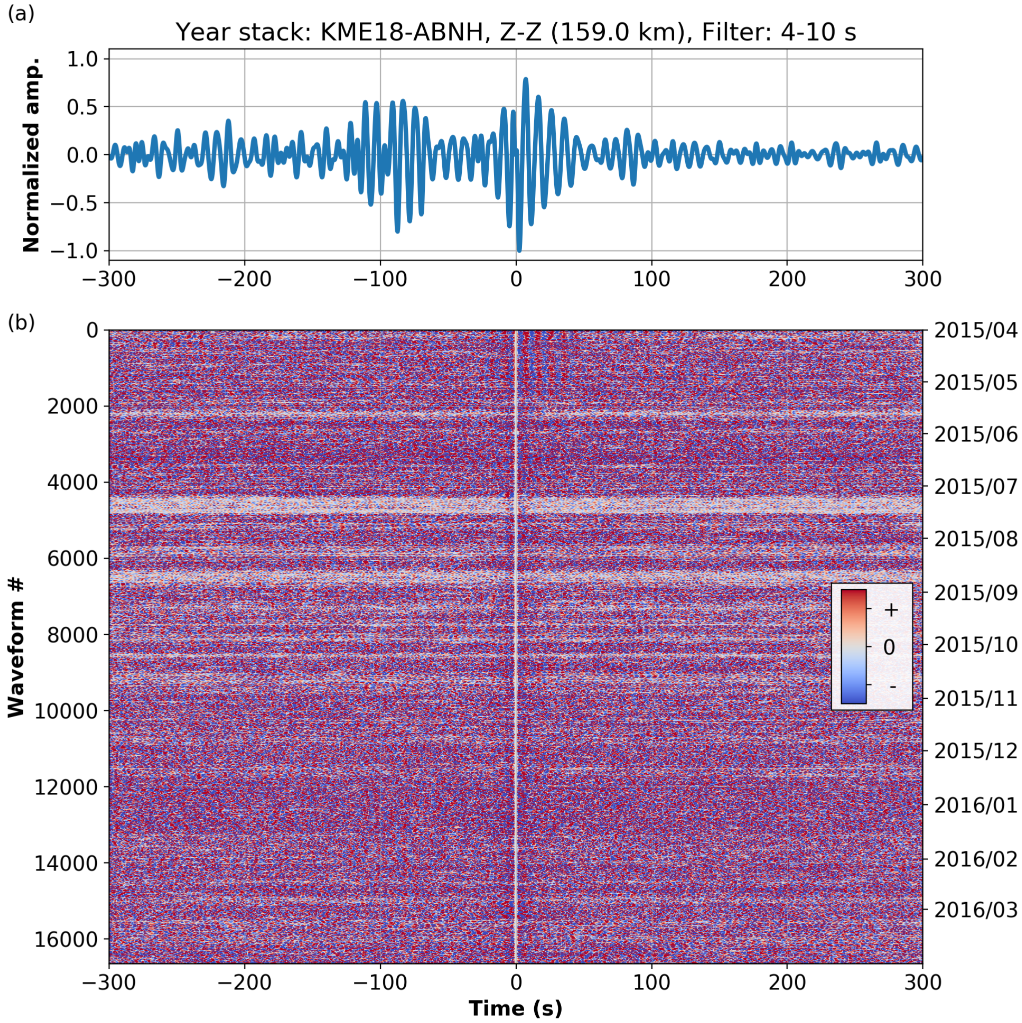

Figure 4. (a) Raw stack over the year of the 30-min deconvolution functions (DFs) between the KME18 and ABNH stations (location in Figure 3) for the Z–Z component. The amplitude of the waveform is normalized in this plot. (b) The 16,641 30-min DFs calculated between April 1, 2015 and March 31, 2016. All the waveforms are bandpass filtered between 4 and 10 s.

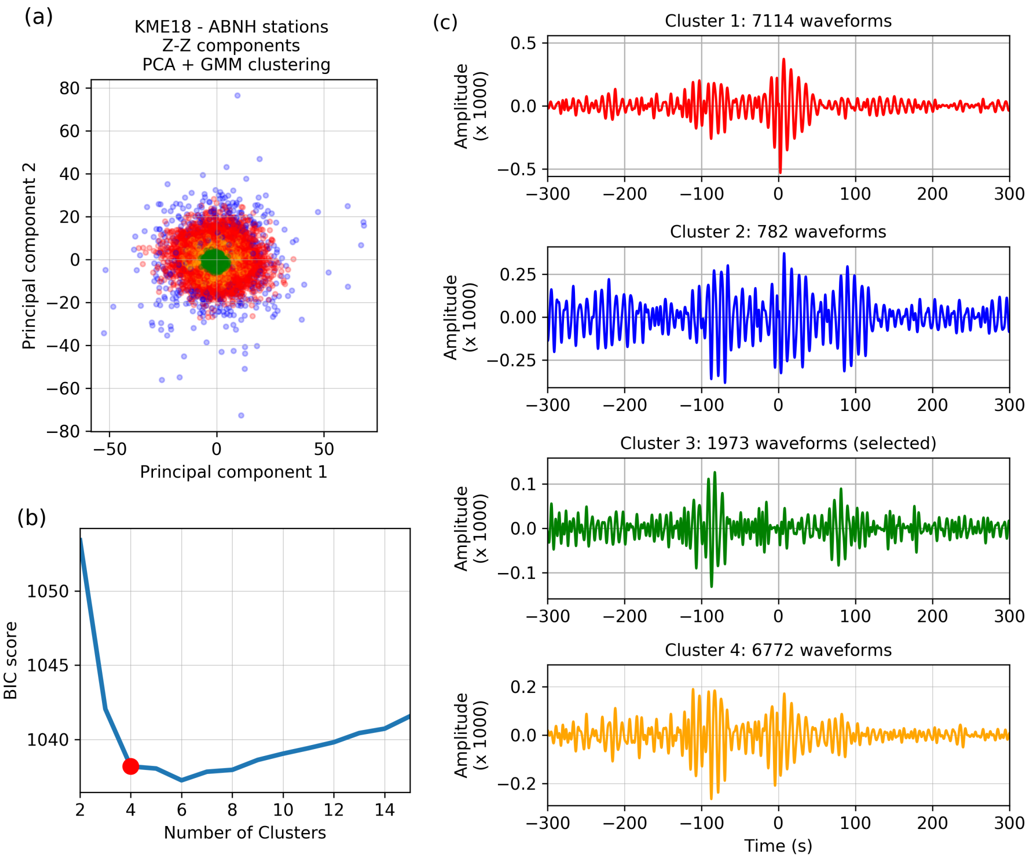

Figure 5. (a) Projection of the 16,641 Z–Z DFs between the KME18 and ABNH stations on the first two principal components of the PCA. The four colors correspond to the clusters obtained with the GMM. (b) BIC score for GMMs performed on the output of the first 10 PCs with different numbers of clusters. The knee method determines that four clusters is optimal (red dot). (c) Stack of the 30-min DFs belonging to each cluster shown in (a). The colors of the waveforms correspond to the colors in (a). Our method automatically selects the Z–Z DF from cluster 3 for this station pair.

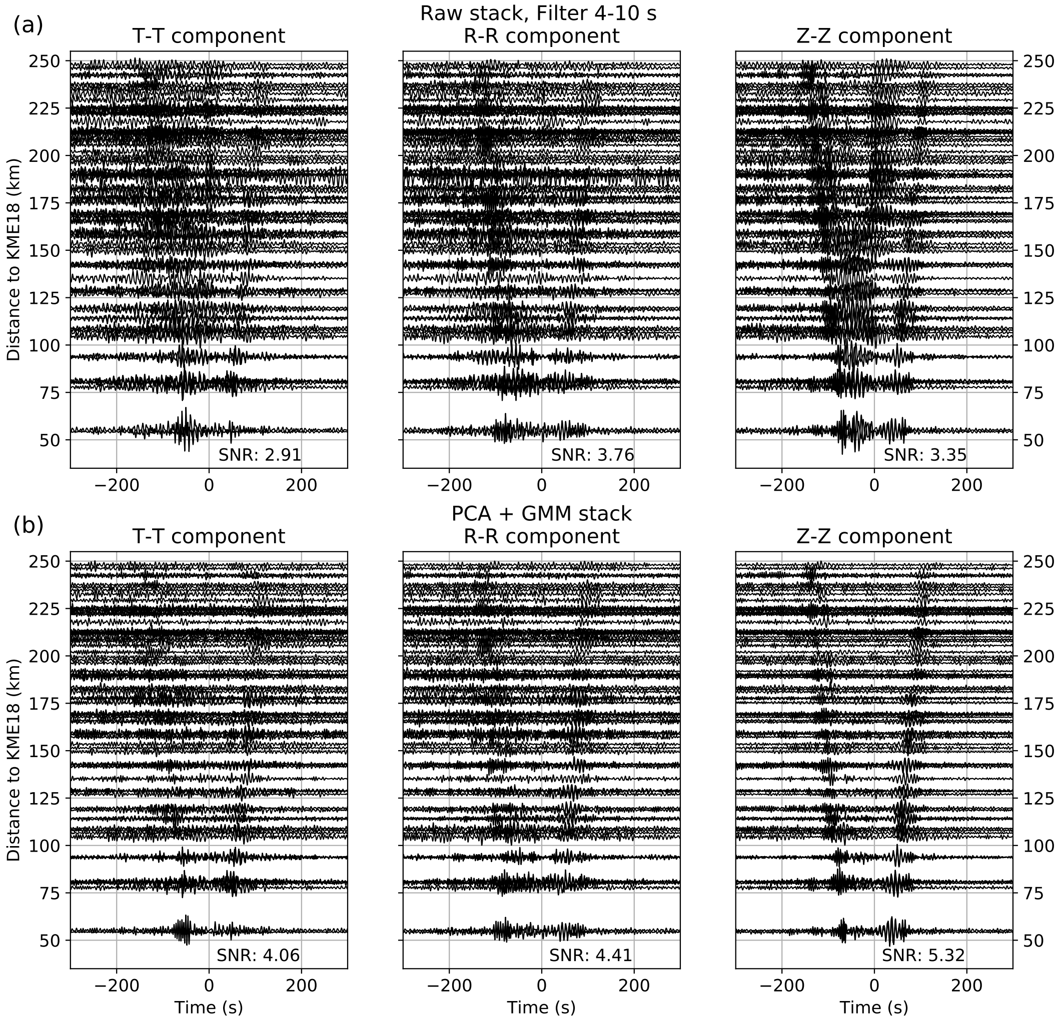

Figure 6. (a) Moveout of the raw stack of the correlation functions for the T–T, R–R, and Z–Z components, band-pass filtered between 4 and 10 s. (b) Same as (a) for the DFs obtained with our two-step clustering method using the first 10 PCs. For each panel, the average SNR (e.g., average value over the anti-causal and causal parts and over 76 stations) is also indicated.

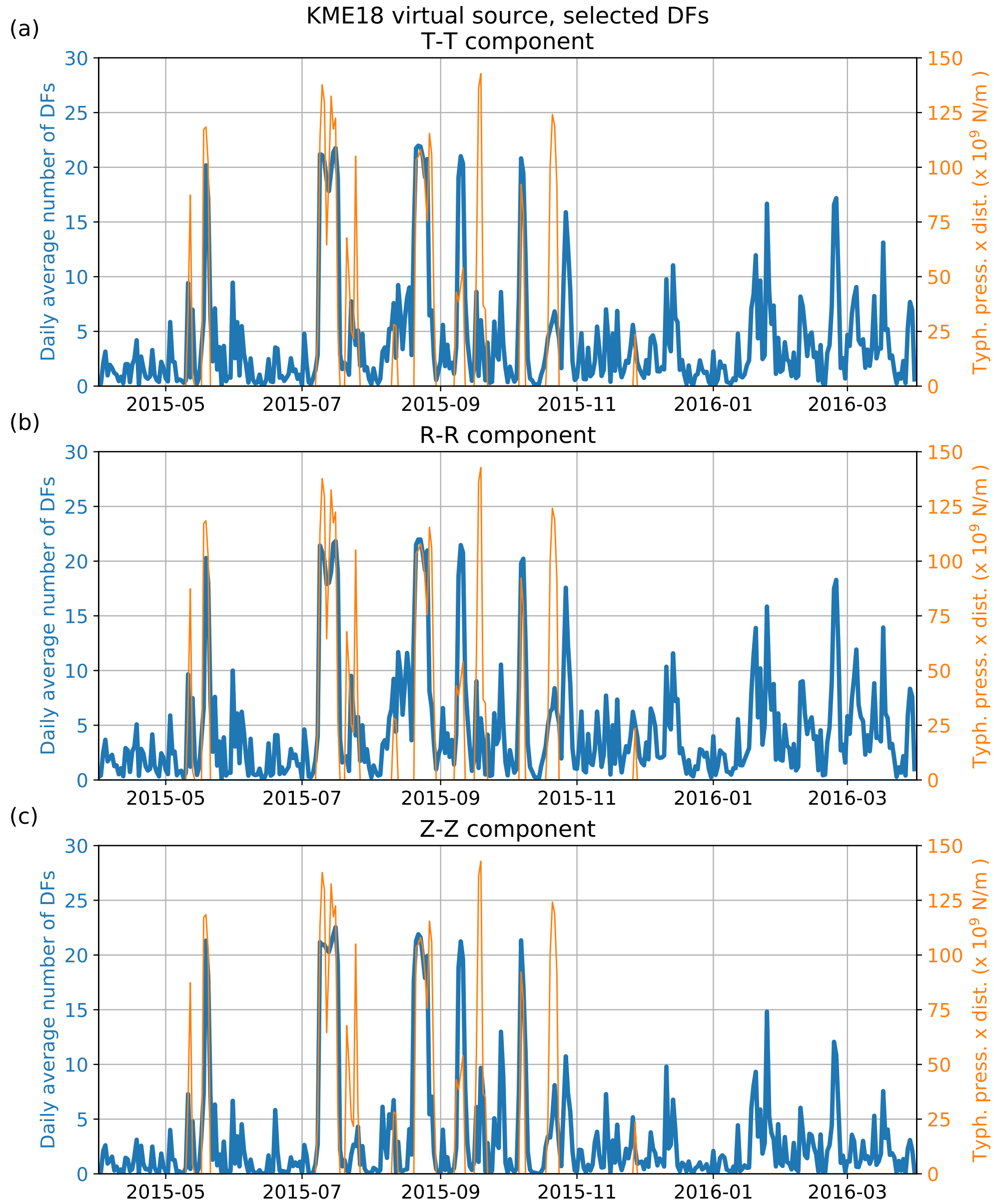

Figure 7. (a) Daily average number of T–T DFs obtained with our two-step method between the KME18 and 77 Hi-net stations (blue). The metric used to investigate the impact of extreme meteorological events on the results (e.g., atmospheric pressure at the center of each storm multiplied by its distance to the the KME18 station) is shown in orange. (b) and (c) are same as (a) for the R–R and Z–Z DFs, respectively.

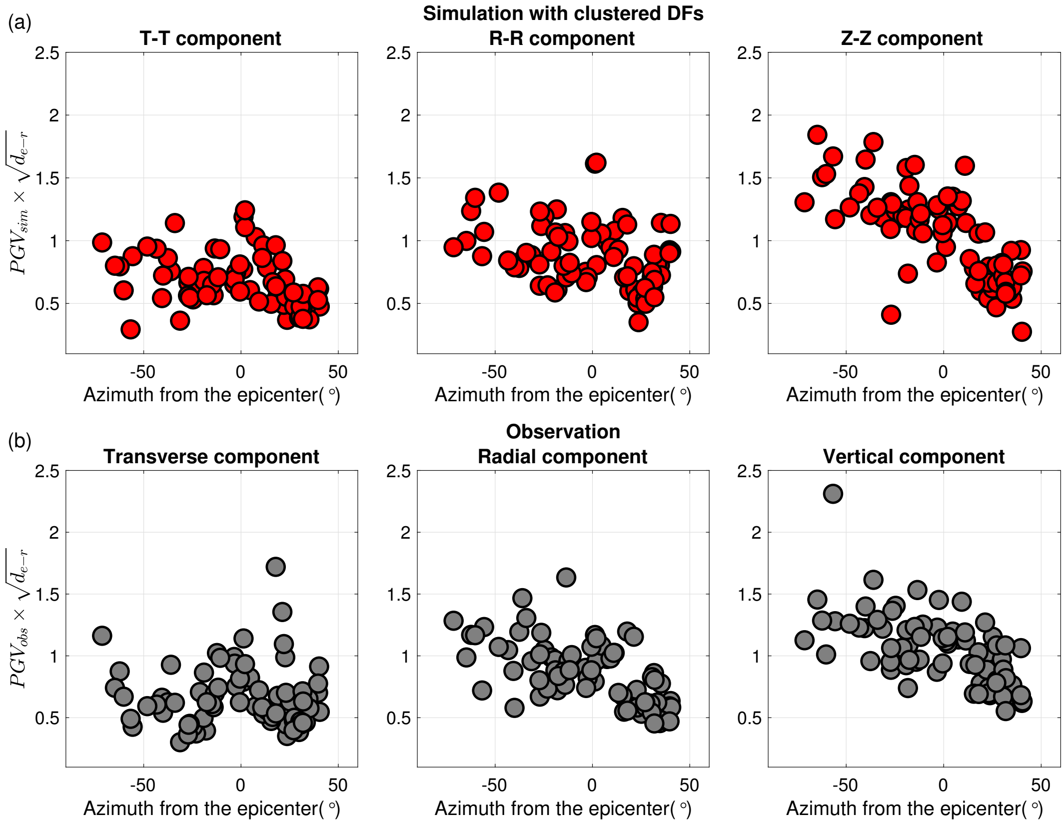

Figure 8. (a) Long-period peak ground velocities of the simulated waveforms ($\mathrm{PGV_{sim}}$) using the T–T, R–R, and Z–Z DFs obtained with the PCA and GMM clustering method (clustered simulations), as a function of the azimuth from the epicenter. The PGVs are corrected for the surface-wave geometrical spreading between the epicenter and receiver locations (e.g., multiplication by $\sqrt{d_{e-r}}$). (b) Long-period peak ground velocities of the 2016 M_w 5.8 earthquake ($\mathrm{PGV_{obs}}$) for the transverse, radial, and vertical components after surface-wave geometrical spreading correction, as a function of the azimuth from the epicenter. The PGV values are computed for seismic waves traveling slower than 3.5 km/s to focus on surface-wave amplitudes and the zero azimuth is north.

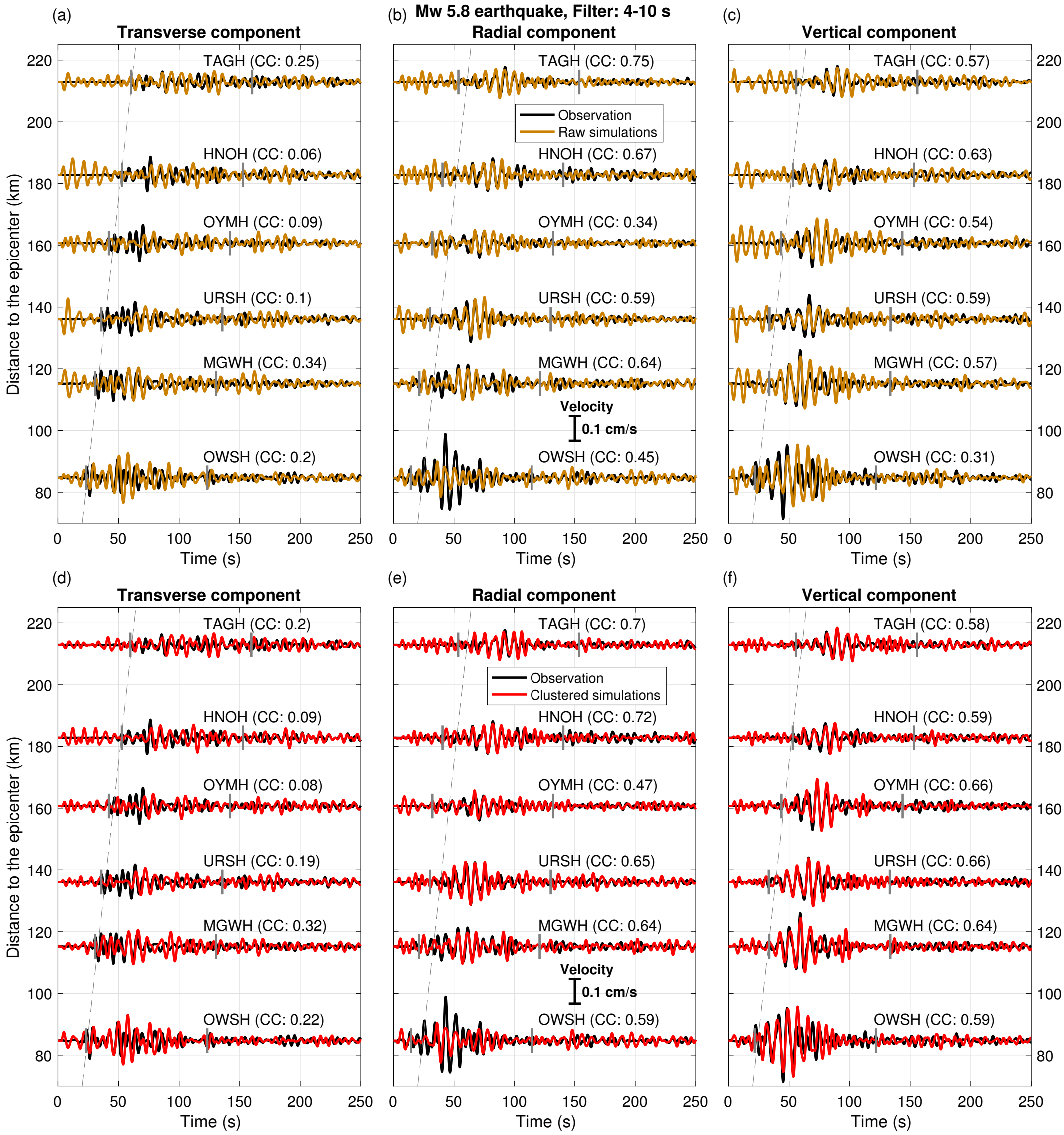

Figure 9. Comparison between simulated and observed (black waveforms) velocity waveforms for the M_{w} 5.8 earthquake for the transverse, radial, and vertical components in the 4 to 10 s period range. The raw simulations are shown by the orange traces in Figure 9a–c and the clustered simulations are shown by the red traces in Figure 9d–f . The location of the stations is shown in Figure 3. For each station, the correlation coefficient (CC) between the simulated and observed waveforms is calculated between the two vertical gray lines and its value indicated between parenthesis. The dashed lines are the 3.5 km/s moveout.

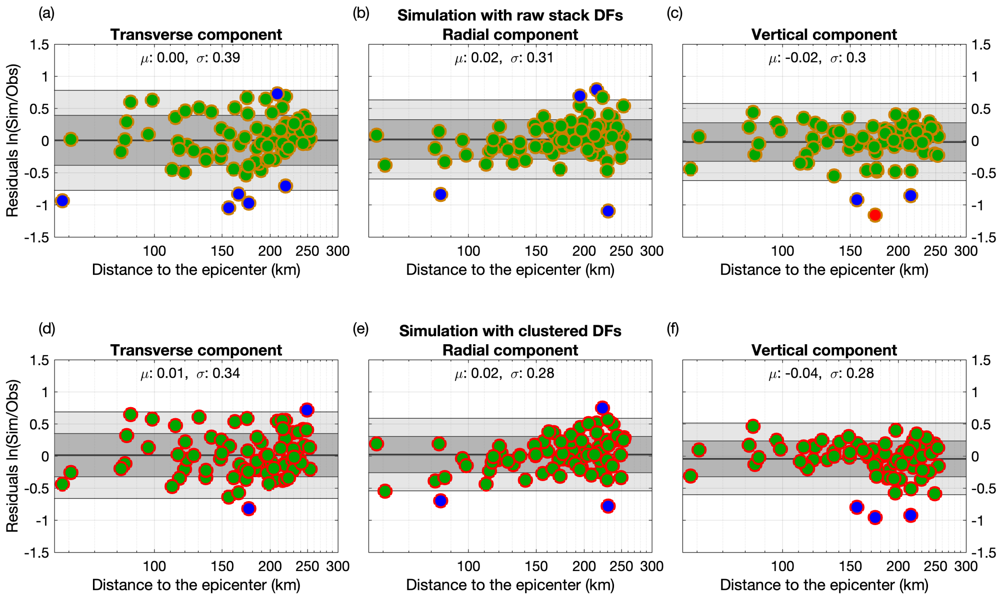

Figure 10. Long-period PGV residuals for the transverse, radial, and vertical components as a function of the distance to the epicenter of the M_w 5.8 event. The raw and clustered simulations are used in Figure 10a–c and Figure 10d–f, respectively. Green circles indicate that the ratio between the simulated and observed PGVs is within a factor of 2 and blue circles show ratio values larger than a factor of 2 but within a factor of 3. The red circle represents a ratio larger than a factor of 3. The thick black line represents the mean of the data, and the 1 and 2 standard deviations to the mean are shown by the dark gray and light gray areas, respectively. The mean of the PGV residuals (μ) and the one standard deviation to the mean (σ) value are shown on top of each panel.

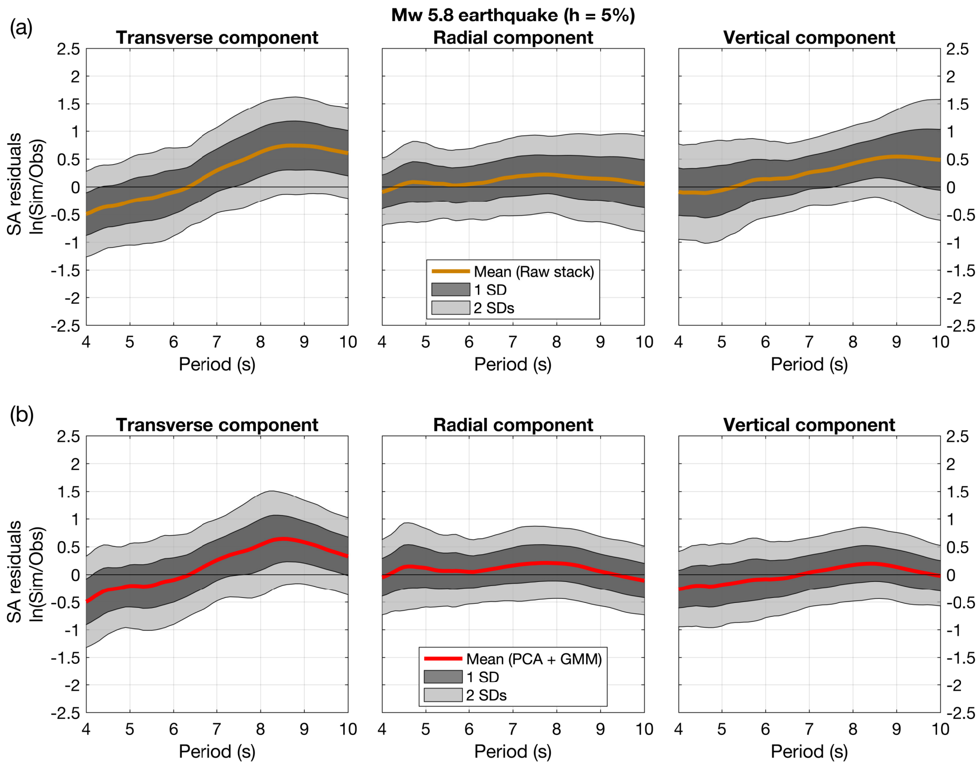

Figure 11. (a) Five-percent damped spectral acceleration (SA) residuals computed between the raw simulations and the observed waveforms of the M_w 5.8 earthquake over the 77 Hi-net stations for the transverse, radial, and vertical components. (b) Same as (a) for the clustered simulations. For each panel, the mean of the SA residuals (red) is shown together with the one (dark gray area) and the two (light gray area) standard deviations to the mean. The zero bias is shown by the black straight lines.

Supporting Information for "Improving the retrieval of offshore-onshore correlation functions with machine learning"

Loïc Viens[1] and Tomotaka Iwata[1]

[1]Disaster Prevention Research Institute, Kyoto University

Contents of this file

Introduction

The supporting information includes:

1. information about the number of principle components kept before performing the clustering.

Text S1: On the number of principle components

In the main manuscript, we compute the PCA of each offshore-onshore deconvolution function (DF) dataset and keep the first $n = 10$ principle components (PCs) before performing the clustering on the low-dimensional space. To determine the appropriate number of PCs needed to retrieve clean DFs after clustering, we tried to keep the first 2, 5, 10, 15, 20, and 25 PCs. For each number of PCs, we compute the DFs using our two-step clustering method. To determine the best number of PCs to perform the clustering, we compute a signal-to-noise ratio (SNR) value for each component (e.g., T–T, R–R, and Z–Z) the same way as detailed in Section 3.2 of the main manuscript. We show the SNR values for each component and the average over the three components in Table S1. While keeping the first 2 PCs only allows us to slightly improve the SNR compared to that from the raw stack of the waveforms, keeping the first 5 or more PCs allows us to significantly increase the SNR values. For our dataset, the highest average SNR is obtained when the clustering is performed on the output of the first 10 PCs, which is why we use this number in the main manuscript.

Method	T–T SNR	R–R SNR	Z–Z SNR	Average SNR
Raw stack	2.91	3.76	3.35	3.34
2 PCs	3.38	3.77	3.90	3.68
5 PCs	4.16	4.40	5.12	4.56
10 PCs	**4.06**	**4.41**	**5.32**	**4.60**
15 PCs	4.01	4.34	5.33	4.56
20 PCs	4.01	4.31	5.10	4.47
25 PCs	3.96	4.34	5.12	4.47

Table S1. SNR of the T–T, R–R, and Z–Z DFs averaged over 76 receiver stations. The DFs are obtained from the raw stack over the year and with our two-step clustering method using different numbers of principle components (PCs). The last column is the average SNR value over the three components.